# Targeting the geysers on Enceladus by viffing descent through the icy plumes

Yue Sun [a,1], Alex Ellery [b,2,*], Xianlin Huang [a,3]

[a] *Harbin Institute of Technology, 150001 Harbin, PR China*
[b] *Carleton University, Ottawa, Ontario K1S 5B6, Canada*

## Abstract

The ice plumes emanating from the geyser vents at Enceladus' south pole offer an enticing route for direct access to acquire pristine astrobiological samples. Unlike traditional landing scenarios where the location of the landing target is known a priori, we propose that one or more penetrators explore the plume environment via lateral maneuvers during the descent to Enceladus' surface to infer the location of promising landing sites by autonomously measuring the plume ice/vapour concentration at multiple locations within the plume. This offers the prospect of targeting the vent sources of the plumes for direct access to subsurface material prior to its ejection. We examine four types of "viffing" (vector-in-forward flight) descent profiles and the impulsive velocity increment ($\Delta V$) required for the lateral maneuvers: (i) a ballistic descent trajectory with a minimal $\Delta V$ cost represents the reference trajectory that implements no lateral search maneuvers; (ii) a planar descent with a decaying lateral oscillation which has an intermediate $\Delta V$ cost and a small search area; (iii) a nested series of decreasing sized box trajectories offering intermediate $\Delta V$ costs of varying degrees depending on the specific parameters; and, (iv) a quasi-spiral trajectory of decreasing radius which imposes the highest $\Delta V$ cost but with the largest lateral search area. Computations and simulations determined that the proposed viffing maneuvers are feasible and permit accurate targeting of Enceladian geyser vents at modest cost in $\Delta V$. We also briefly assessed the problem of mapping the Enceladian plume during the descent, which will ultimately be necessary for viffing.

© 2020 COSPAR. Published by Elsevier Ltd. All rights reserved.

* Corresponding author at: Carleton University, Ottawa, Ontario K1S 5B6, Canada.

*E-mail addresses:* yuesun8@cunet.carleton.ca (Y. Sun), alexellery@cunet.carleton.ca (A. Ellery), xlinhuang@hit.edu.cn (X. Huang).

[1] Doctoral Candidate, Centre of Control Theory and Guidance Technology, School of Astronautics, No. 92, Dazhi W Street, Harbin, Heilongjiang, PR China; currently Visiting Doctoral Student, Mechanical and Aerospace Engineering Department, Carleton University, 1125 Colonel By Drive, Ottawa, ON K1S 5B6, Canada.

[2] Associate Professor, Mechanical and Aerospace Engineering Department, 1125 Colonel By Drive, Ottawa, ON K1S 5B6, Canada.

[3] Professor, Centre of Control Theory and Guidance Technology, School of Astronautics, No. 92, Dazhi W Street, Harbin, Heilongjiang, PR China.

## 1. Introduction

Enceladus is a moon of Saturn with a 500 km diameter covered by a global ice surface. The Cassini spacecraft through several flybys from 2005 to 2010 confirmed that there are liquid water reservoirs beneath its ice crust (Krupp et al., 2012). Water ice particles and water vapour are emitted from cryovolcanism at the south pole area (marked by fissures known as "tiger stripes") (Geissler, 2015). Most of the ice particles fall as snow from the plumes onto the surface, making Enceladus one of the most reflective bodies of the solar system (Jost et al., 2018). These cryo-eruptions also supply material to replenish

Saturn's E-ring (Porco, 2006). The existence of subsurface liquid water reservoirs imply submarine hydrothermal activity at a rocky core (Domagal-Goldman et al., 2016) and suggest the possibility of biological activity (Porco et al., 2017). The water-ice plumes originating at the tiger stripes provide enticing opportunities to sample the subsurface ocean in a near-pristine state (Witze, 2014). Consequently, Enceladus is regarded as one of the best locations in the solar system to investigate the prospect for extraterrestrial life (Hargitai and Kereszturi, 2015).

Enceladus is believed to possess a subglacial ocean in contact with a silicate core representing a potential habitat for chemosynthetic life (German, 2004). Internal heating is generated by the synchronously rotating satellite in low eccentric orbit around Saturn. Thermal energy may also be generated through serpentinization $(2Mg_2SiO_4 + 3H_2O \rightarrow Mg(OH)_2 + Mg_3Si_2O_5(OH)_4)$ of ferromagnesian silicate minerals (olivine and pyroxene) in the rocky core thereby driving hydrothermal vents (Vance et al., 2007; Góbi and Kereszturi, 2017). It has been postulated that microbes may reside in the subsurface ocean similar to those in terrestrial hydrothermal vents. There is possible evidence of fossilized microorganisms on Earth from submarine hydrothermal vent deposits dating back between 3.77 and 4.28 billion years ago in Nuvvuagittuq Greenstone, Quebec (Dodd et al., 2017). Viable microorganisms may have been extracted from Antarctic sediments dating back to the Pliocene-Quaternary, approximately 2.5 million years ago (Gilichinsky et al., 1992). These microorganism fossils are 0.5 mm long by 10 $\mu$m wide hematite filaments reminiscent of Fe-oxidizing bacteria associated with 50–200 $\mu$m carbonate rosettes with embedded C-13 depleted graphite inclusions. These deposits are quite different from the disputed "conical" stromatolite deposits of postulated photosynthetic cyanobacteria in the 3.7 billion year old Isua supracrustal belt in Greenland (Allwood et al., 2018).

On Enceladus, evidence of life from the subsurface ocean, if it exists, may be ejected into space via the ice plumes which erupt from the four ice fissures (tiger stripes) at the south pole area (Barge and White, 2017). The plumes contain molecular hydrogen (possibly derived from hydrothermal activity), carbon dioxide and organic material including complex organic molecular masses exceeding 200 amu (Postberg et al., 2018). It is reckoned that the organics may come from an organic film below the ice that originated from rising gases released from the silicate core (Postberg et al., 2011). However, any ejected microbes in the plumes would be altered by their exposure to space – this places a premium on landing as close to the tiger stripe fissures as possible.

The geysers emanating from Enceladus' tiger stripes area and the fresh material that falls back onto the surface (Jost et al., 2018) are considered the foremost locations to acquire pristine organic samples (Postberg et al., 2011). Missions that focus on examining the material in the icy

plumes (Coustenis et al., 2009; Konstantinidis et al., 2015) would be a boon for scientific research (Kereszturi, 2018; Porco et al., 2017). Much of the technology developed for exploring Enceladus may be applied to other icy targets e.g., Europa (McKay, 2008) and Titan.

We are investigating the prospect of deploying scientific instruments within Enceladus' subsurface using one or more penetrators (Kereszturi and Keszthelyi, 2013). A planetary penetrator is a cylindrical spacecraft designed to impact and penetrate into a solid target using its kinetic energy (Lorenz, 2011; Anderson et al., 1996). It is an efficient mechanism for delivering scientific instruments beneath the surface of the target body (Gowen et al., 2011), making penetrators the most suitable vehicle for the subsurface exploration of Enceladus. Penetrators have the advantage of low mass yet tolerate hard impacts with minimal fuel consumption, when compared to a traditional lander mission (Raus et al., 2012). In our case, it is desirable for the Enceladus penetrator to map the plume continuously to target the plume source (Grygorczuk et al., 2011). Therefore, the trajectory profile is crucial for the collection of informative data about the plume — it is this aspect that is addressed here.

We analyze a flyby orbit of Enceladus and compare the impact trajectories based on a single plume model. We use simulation assumptions including calculations of Enceladus' sphere of influence, the impact velocity of the penetrator, and a single-plume regression model. We define and simulate four types of viffing descent and impact trajectories, including a ballistic trajectory (which acts as the reference trajectory), a planar decaying oscillation trajectory, a hybrid trajectory of nested boxes, and a quasi-spiral trajectory.

## 2. Simulation model assumptions

Enceladus is a moon of $1.08 \times 10^{20}$ kg mass with an average radius of 252.1 km (and a slightly smaller 248.33 km polar radius). Its orbit around Saturn has a semi-major axis of 237 948 km and an eccentricity of 0.0047. Enceladus' gravitational field is dwarfed by Saturn's gravitational field, which perturbs the spacecraft orbiting around Enceladus resulting in extra orbital maneuvers to maintain stable orbits. We calculated the Enceladus gravitational field, the impact velocity of a penetrator, and the descent profiles through the icy plume. In order to target one of these sources, a mother spacecraft, like Cassini, would be required to release a penetrator and its propulsion system during its flyby of Enceladus. After interception with the plume, the penetrator would separate from the propulsion system at a suitable altitude, and then explore the plume environment. These operations would be guided by an online source localization algorithm to finally impact the source. We define the longitudinal descent profile as free fall from Enceladus' sphere of influence. We show that the proposed free fall strategy

guarantees an effective impact depth with minimal fuel consumption.

## 2.1. The sphere of influence

The sphere of influence (SOI) is defined as an oblate-spheroid-shaped region around a celestial body within which the primary gravitational influence on an orbiting object is that body. Outside the SOI, other celestial bodies' gravitational fields also affect a spacecraft's orbit. The radius of the sphere of influence, $r_{SOI}$, assuming a spherical gravitating body is given by

$$r_{SOI} \approx a\left(\frac{m}{M}\right)^{2/5} \tag{1}$$

where $a$ is the semi-major axis of the orbit of a small body with mass $m$ around a large body with mass $M$. According to Eq. (1), Saturn's radius of its SOI around the Sun is $54.6 \times 10^6$ km, which encompasses Enceladus within Saturn's gravitational dominion. The radius of Enceladus' SOI around Saturn is 456.22 km, which means that within an altitude of 208 km from Enceladus' surface, Saturn's gravity can be ignored. This defines the highest altitude for the release of an Enceladus penetrator. At any higher altitude, Saturn's gravity would perturb the trajectory of the penetrator.

The penetrator would free fall from the SOI to attain its required impact velocity but employs lateral thrusting to map the plume as it descends. If the freefall impact velocity is insufficient to penetrate to the desired depth into the surface ice (nominally 0.2to1 m), extra thrust would be required. We also impose a terminal velocity constraint of 100 to 300 m s$^{-1}$ to ensure that there is no significant physical and thermal distortion to the ice sheath created by the impactor. This protects the pristineness of the icy environment to ensure that there is no corruption to scientific instrument data. We demonstrate that a penetrator free falling from SOI would satisfy our velocity constraint.

The free fall impact velocity may be determined from the law of conservation of mechanical energy ignoring any external forces except gravity,

$$\frac{1}{2}mv_f^2 - \frac{1}{2}mv_0^2 = m\int_{r_0}^{r_f} g\,dr \tag{2}$$

where $m$ is the mass of a penetrator, $v_f$ is the impact velocity, $v_0$ is the initial velocity, $r_f = 248.33$ km = polar radius of Enceladus, and $r_0 = 456$ km = SOI radius. The acceleration due to gravity ($g$) is calculated by Newton's law of universal gravitation,

$$g = \frac{GM}{r^2} \tag{3}$$

where $M = 1.080\,22 \times 10^{20}$ kg kg is the mass of Enceladus, and the universal gravitation constant $G = 6.67 \times 10^{-11}$ m$^3$ kg$^{-1}$ s$^{-2}$. Assuming no external forces, an object free falling from the SOI with initial zero velocity

$v_0$ results in an impact velocity of $v_f = 162.08$ m s$^{-1}$. This lies within the upper bound of the impact velocity constraint. The free fall strategy eliminates the need for fuel consumption in accelerating or decelerating the penetrator. For a 12 kg penetrator with a 0.2 m diameter and a 0.2 m conical nose, the impact depth $D$ is given by the Sandia equation (Young, 1997),

$$D = 0.0000046SN\left(\frac{m}{A}\right)^{0.6}(V - 30.5)\ln(50 + 0.29m^2)$$
$$N = 0.25\frac{L_n}{d} + 0.56 \tag{4}$$

where $S = 2.75 \pm 0.5$ denotes the penetrability of a completely frozen shell of ice, $N$ is the performance of the penetrator nose of diameter $d$ and length $L_n$, $m$ = mass of a penetrator, and $A$ = cross-section of the penetrator. Thus, the terminal velocity constraint will generate a penetration depth of 0.22 to 0.85 m. The ideal penetration depth is determined by two opposing constraints: neither too deep nor too shallow. The depth of penetration into should be as shallow as possible to recover samples from the plume deposits with minimum exposure to space during ejection and surface residence. Simultaneously, the impact depth should be sufficiently deep to acquire stable subsurface samples at the venting source and maximize anchorage for good mechanical coupling to the ice shell.

## 2.2. Free fall time

The duration of flight is an important parameter for developing lateral profiles. If the acceleration due to gravity was constant, the time of free fall $t$ from altitude $h$ can be solved simply by:

$$h = v_0 t + \frac{1}{2}gt^2. \tag{5}$$

However, $g = \frac{GM}{r^2}$ varies from $r_0$ with $g = 0.035$ m s$^{-2}$ to $r_f$ with $g = 0.116$ m s$^{-2}$, i.e. acceleration scenario in which $t$ is difficult to solve even using the dynamic equation $\dot{v} = \frac{GM}{r^2}$. Although $t$ does not have a closed-form solution, it is possible to divide the whole height to $I$ segments assuming that $g$ equals to the constant $\bar{g}_i$ within each segment $i$, from $r_i$ to $r_{i+1}$. The duration $t_i$ of the $i$th segment is given by a closed-form solution:

$$t_i = \frac{v_i - v_{i-1}}{\bar{g}}, \tag{6}$$

where $v_i$ and $v_{i-1}$ are the final velocities of the $i$th and $i-1$th segments determined by the law of conservation of energy. If $\alpha$ represents the changing rate of $g$ from $r_{i-1}$ to $r_i$, $g$ is regarded as a constant if the inequality in Eq. (7) holds:

$$r_i \leqslant \frac{r_{i-1}}{1 + \alpha}. \tag{7}$$

The following algorithm approximates the duration of free fall:

**Input:** $r_0, r_f, G, M, v_0$
**Ouput:**$t_f$
```
1:    Initial i = 1, t = 0, tᵢ = 0, α
2:    while tᵢ > t_f do
3:       rᵢ = r_{i-1}/(1+α)
4:       if rᵢ ≤ r_{i-1} then
5:          rᵢ = r_{i-1}
6:       end if
7:       vᵢ = √(v²_{i-1} + 2GM(1/rᵢ − 1/r_{i-1})⁻¹)
8:       r̄ᵢ = (r_{i-1} − rᵢ)/2
9:       ḡᵢ = GM/r̄ᵢ²
10:      tᵢ = (v̄ᵢ − v_{i-1})/ḡᵢ
11:      i = i + 1
12:      t = t + tᵢ
13:   end while
14:   return t
```

When $\alpha \to 0$, the estimate residual $e_t \to 0$, as verified by the simulations in Section 4.

### 2.3. Icy plume modelling

Cassini flew by Enceladus 14 times from 2005 to 2010 summarized by a graphical representation of Cassini's E5 and E6 trajectories in Fig. 1 and Table 1 (Krupp et al., 2012). The lowest altitude of the flybys was 50 km over the south polar area.

From Cassini's scientific data on water vapour plumes, the average emission velocity of the ejecta of the plume at the surface is measured as 412 m s$^{-1}$, well above the 240 m s$^{-1}$ escape velocity from Enceladus' gravitational influence (Hansen, 2006). This implies that the ejected particles will escape from Enceladus' gravity. The amount of ejected material escaping from Enceladus at a radial distance of ¸2000 km has been estimated at 93 kg s$^{-1}$ consistent with the measurements of Cassini (Waite, 2006).

Saur et al. (2008) developed a single-plume regression model using Cassini data. The single-plume model defines the plume density at a longitude of 292.5° given by:

$$C = C_0 \left( \frac{R_E}{h + R_E} \right)^2 \exp \left[ -\left( \frac{\Theta}{H_\Theta} \right)^2 \right] \exp \left( \frac{h}{H_d} \right), \qquad (8)$$

where $h$ = altitude, $\Theta$ = angular distance from the plume centre, $C_0 = 2.7 \times 10^9$ cm$^3$ = density at the centre of the plume on the Enceladus' surface, $R_E = 248\,329$ m = radius of Enceladus, $H_\Theta = 12°$ = angular width of the plume, and $H_d = 3792$ km = four times the radius of Enceladian Hill sphere. The model predicts that the height of the plume must exceed 750 km, implying that the radius of SOI lies only 1/3 the height of the plume.
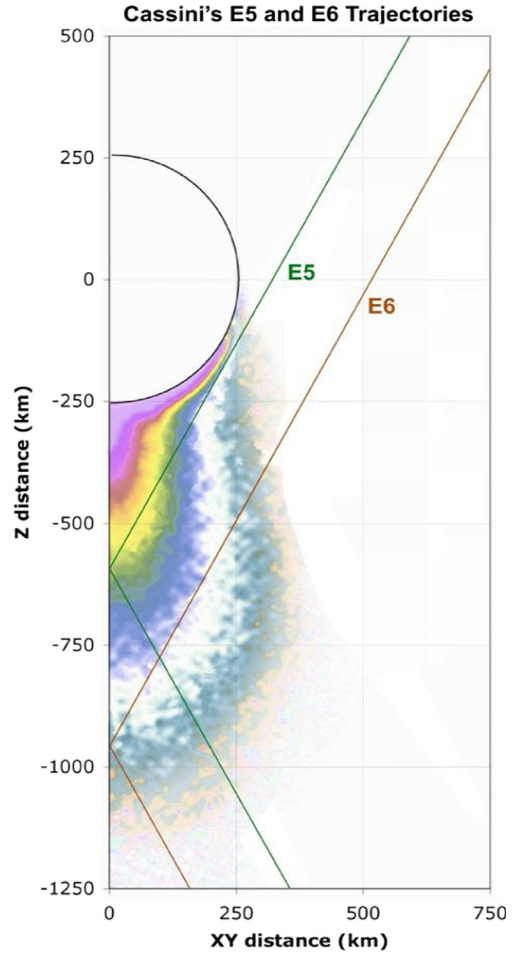


Fig. 1. Cassini's E5 and E6 flybys of Enceladus (Krupp et al., 2012). The x and y axes represent the distance from Enceladus' centre of mass, while the colour contour represents the plume flow field. (For interpretation of the references to colour in this figure legend, the reader is referred to the web version of this article.)

Table 1
Cassini's Enceladus flybys during 2008 to 2012 showing time, closest distance above the south pole area, and the type of the encounter.

| Flyby | Time | Closest Distance (km) | Type |
|-------|------|----------------------|------|
| E0 | 2005.048 | 1260 | Equatorial north |
| E1 | 2005.068 | 497 | Equatorial north |
| E2 | 2005.195 | 166 | High latitude |
| E3 | 2008.072 | 48 | High latitude |
| E4 | 2008.224 | 49 | High latitude |
| E5 | 2008.283 | 25 | High latitude |
| E6 | 2008.305 | 169 | High latitude |
| E7 | 2009.306 | 99 | Equatorial south |
| E8 | 2009.325 | 1680 | Equatorial south |
| E9 | 2010.118 | 99 | Equatorial south |
| E10 | 2010.138 | 434 | Equatorial south |
| E11 | 2010.225 | 2550 | Equatorial south |
| E12 | 2010.334 | 48 | Equatorial south |
| E13 | 2010.355 | 48 | Equatorial south |

## 3. Mission concept

### 3.1. Mission sequence

The following simulation model is performed using the astrogator toolbox of Satellite Toolkit (STK) with an Enceladus-centric reference frame. Before developing the viffing trajectories, we proposed a mission sequence shown in Fig. 2a and b.

During an Enceladus flyby, a Cassini-like mother spacecraft is assumed to release a penetrator propulsion system at an arbitrary Enceladus-centric distance of 500 km modelled by STK. The flyby orbit (the green line in Fig. 2b) of the mother spacecraft is simulated as a 2000 km circular polar orbit around Enceladus, shown in Table 2. The right ascension of ascending node is 90°, while the argument of periapsis and the true anomaly of the orbit are both determined by STK.
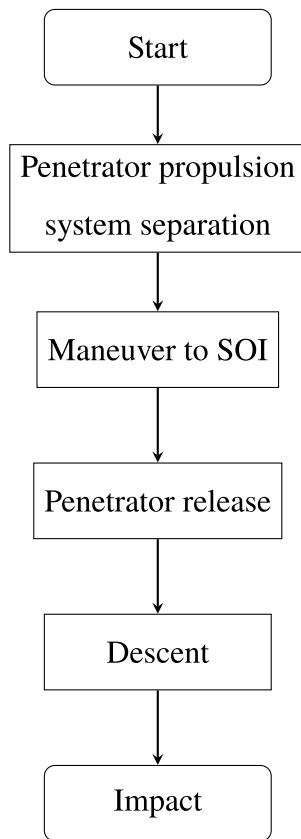
The penetrator propulsion system has a 153.5 m s$^{-1}$ initial velocity deorbits from the mother spacecraft's flyby orbit deploying the penetrator into the SOI altitude and shedding its initial velocity (the red line in Fig. 2b). Ideally,

Table 2
Keplerian elements of the assumed flyby orbit including semi-major axis (from the mass centre), eccentricity, inclination, right ascension of the ascending node, argument of periapsis, and true anomaly. The initial orbit is assumed to be a circular polar orbit.

| Elements | Value |
|---|---|
| Semi-major axis | 2000 km |
| Eccentricity | 0 |
| Inclination | 90° |
| Right ascension of ascending node | 90° |
| Argument of periapsis | determined by STK |
| True anomaly | determined by STK |

this will give the penetrator a 0 m s$^{-1}$ initial velocity vertically to give the penetrator as much time as possible to conduct its lateral maneuvers. Thus, the penetrator propulsion system requires 153.50 m s$^{-1}$ $\Delta V$ for a braking burn which dominates the total $\Delta V$ requirement compared to the subsequent descent maneuvers. Simultaneously, the penetrator must perform a de-spinning maneuver to give the penetrator a 0 rad s$^{-1}$ rolling angular velocity to permit it to engage in lateral maneuvers. Once inserted into the SOI, the two-body force (between the penetrator and Enceladus)



(a) Mission flowchart
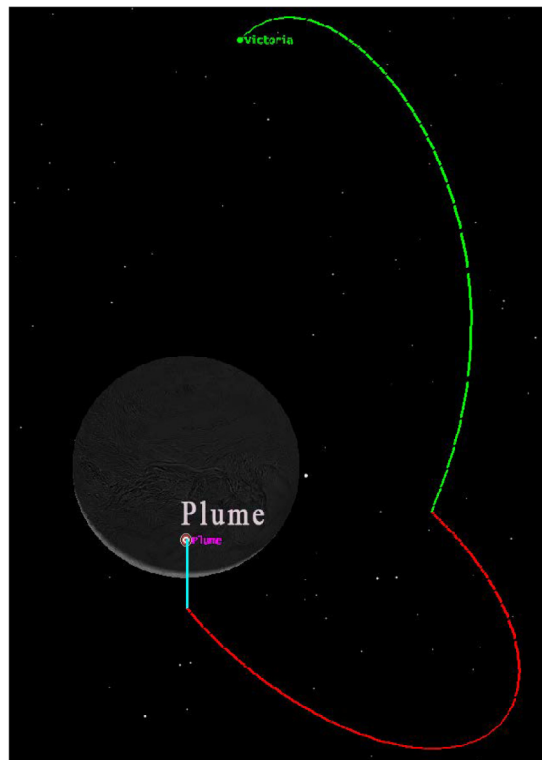
(b) Mission schematic graph.

Fig. 2. Mission sequence flowchart and schematic graph. A mother spacecraft releases a penetrator propulsion system on its flyby orbit (green line in (b)). The penetrator propulsion system deploys a penetrator into the sphere of influence (SOI) of Enceladus and shed its initial velocity before separation of the propulsion system (red line in (b)). After release, the penetrator free falls and searches the plume environment through lateral maneuvers, and locates the plume source during the descent (blue line in (b)). Finally, the penetrator impacts into the plume source to conduct the scientific operations. (For interpretation of the references to colour in this figure legend, the reader is referred to the web version of this article.)

is the only gravitational force applicable. An Enceladus inertial coordinate system is adopted during the descent. In the descent phase (the blue line in Fig. 2b), the penetrator measures the plume concentration continuously to model its structure and thereby locate the source. It impacts the Enceladus ice shell in or near a plume source vent as determined by its estimation source location.

To ensure the 12 kg impact mass, we assume that all propellant has been consumed prior to and during the descent. The penetrator free falls to attain the desired impact velocity no vertical maneuvers are required. STK computes the required initial fuel mass with thruster parameters shown in Table 3.

Once in the plume, the penetrator must locate of the source by measuring the plume concentration during the descent. It is assumed that the penetrator use a Humicap, an off-the-shelf humidity detector, to measure water vapour concentration and a quartz microbalance or surface acoustic wave sensor to measure the impact of ice particles. This provides a measure of ice/vapour density within the plume. Hence, the penetrator builds a plume source likelihood map (SLIM) to estimate the source location used to guide the penetrator to the target area.

Following impact and penetration into the ice, the scientific mission commences. Scientific payload instruments are assumed mounted on the front of the penetrator which would be deployed once delivered into the ice subsurface. The penetrator may analyze the morphological and mineralogical characterization of the ice, detect and quantify evolved gases on heating and characterize organic components (using miniaturized Raman spectroscopy and/or Nanopore technology) for 7 days. The penetrator must nominally survive in a low power state for another 3 days to transmit its data to the mother spacecraft on its subsequent flyby.

### 3.2. Enceladus penetrator

Before developing lateral maneuvers, we consider a dynamic model of the penetrator implemented in our simulations. Planetary penetrators are missile-shaped spinning probes designed to penetrate solid surfaces at impact. Fig. 3 shows a typical design. The 6-DOF dynamic model of a penetrator is outlined in Appendix A(Zipfel, 2007).

According to the dynamic model, the attitude dynamics and the trajectory dynamics are coupled because of continuous rolling motion. Theoretically, only one pair of

Table 3
Simulated thruster parameters including thruster tank pressure, tank temperature, fuel density, and engine $I_{sp}$.

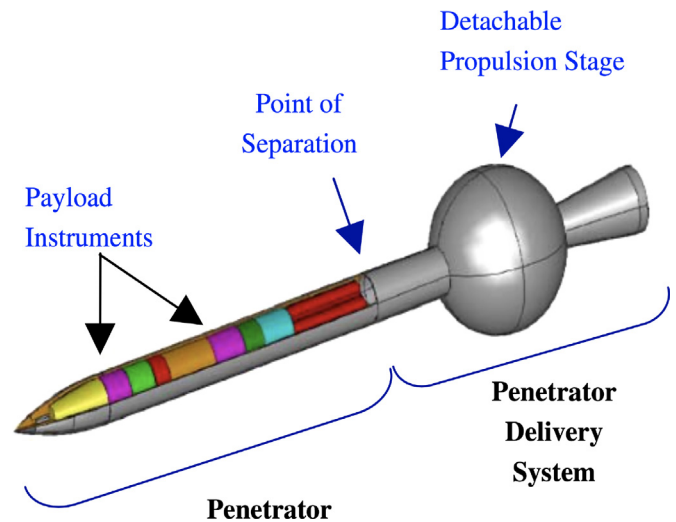| Parameter | Value |
|---|---|
| Tank Pressure | 500 Pa |
| Tank Temperature | 293.15 K |
| Fuel Density | 1000 kg m$^{-3}$ |
| $I_{sp}$ | 300 s |



Fig. 3. Conceptual design of Enceladus penetrator of the cancelled TandEM (Titan and Enceladus Mission) (Coustenis et al., 2009). Payload instruments (e.g. descent detectors and scientific instruments) are mounted on the front, which would be deployed into the icy shell.

thrusters can control all 6-DOF dynamics of the penetrator. However, the rolling motion not only imposes a complex non-linear segment into the dynamics but it also reduces the maneuverability of the penetrator because of the gyroscopic stiffness of the spin. Therefore, the penetrator must de-spin. The penetrator employs a group of 4 orthogonal thrusters to provide trajectory maneuvers through the centre of mass and another group of 4 thrusters to provide three-axis attitude stabilization torques. These thruster sets decouple the attitude control loop from the trajectory control loop so that the magnitude of the attitude torques are negligible in comparison with the trajectory thrust magnitudes. Therefore, the penetrator can be regarded as a point mass governed by the trajectory dynamic equations in the simulations.

We assume that a detachable penetrator propulsion system is separated from the penetrator before the descent. The penetrator nose points in the nadir direction without spinning so its attitude is maintained by three-axis attitude stabilization while the viffing maneuvers are implemented by the trajectory control system.

## 4. Lateral trajectory strategies

Traditional viffing employs vectoring of thrust engines to alter the direction of thrust on a vertical/short take-off and landing (V/STOL) aircraft such as the Harrier jumpjet (Gal-Or, 1990). Thus, the vectored torques and controlled aerodynamics greatly improve the lateral maneuverability of the aircraft (Gal-Or, 1990). Viffing has a wide range of applications in military V/STOL aircraft such as dogfighting faster aircraft and rolling landings on aircraft carriers (Ikaza, 2000), but they are unsuitable for direct space applications where aerodynamics are absent (Flamm et al., 2007). Hence, penetrator viffing maneuvers

are implemented by lateral thrusters which provides thrust that passes through the vehicle's centre of mass but not torques.

From the perspective of guidance and control, there are two ways to perform viffing maneuvers. One is to devise a trajectory online and track its progress until impact while the second is to generate a sequence of waypoints which define the turning points of the trajectory to chart the trajectory. The greater the demands imposed on the accuracy of trajectory tracking, the greater the fuel consumed since trajectory tracking requires frequent closed-loop control efforts. For Enceladus plume mapping missions, the purpose of trajectory tracking is to guide the vehicle for data measurement rather than achieving a minimum trajectory flight from orbit to target. Trajectory tracking is thus not an appropriate approach for plume mapping particularly given the constraints imposed by propellant consumption. However, the waypoint method has no accurate tracking requirements which is more fuel efficient for plume mapping missions. The onboard computer calculates a sequence of waypoints based on the flight status and the estimated target location and then corrects these waypoints after updating the estimated target. Although a waypoint strategy covering a larger search area yields a better estimation, fuel consumption is also increased when the estimation error decreases. Therefore, fuel consumption - $\Delta V$ costs - becomes the primary evaluation standard of a trajectory.

In order to examine different viffing profiles, we simulated four types of waypoint trajectories: a ballistic trajectory, a planar descent trajectory, a trajectory of nested boxes and a quasi-spiral trajectory. The following simulations illustrates that the ballistic trajectory requires the minimal $\Delta V$ costs with no lateral search; the planar trajectory search in a viffing plane imposes intermediate $\Delta V$ costs; the trajectory of nested boxes also offers intermediate $\Delta V$ costs but varying degrees depending on the search space, and the quasi-spiral trajectory imposes the highest $\Delta V$ costs with the largest search area.

### 4.1. Ballistic trajectory

The ballistic trajectory is a direct impact strategy whereby the penetrator impacts the estimated plume source without any search maneuvers - it constitutes our reference trajectory. No exploration is employed during the descent which can be open loop or closed loop. Although we assume open loop reference trajectories here, lateral maneuvers could potentially be employed with infrared cameras sensitive to hot spots to eliminate source localization error visually. Compared with other viffing trajectories that we shall present, fuel consumption for the ballistic strategy is minimal even with minor error corrections. The amount of data measured using onboard detectors is also minimal since no lateral searches are employed so that plume mapping efficiency is poor. Consequently, the accuracy of plume source localization will be highly error prone

and the value of the impact site will be diminished (Fig. 4, Table 4). We assume that the plume source is located at Enceladus' south pole and that the release point of the penetrator is directly above the source, making the ballistic trajectory almost a straight line. The plume source location may be randomly located but this imposes the same $\Delta V$ costs.

The discrepancy between the simulated free fall time (3171 s) and the theoretical computation (3173 s) is due to STK's gravity field model being more accurate than the simplistic equations of Eq. (3) for the variation of $g$.

### 4.2. Planar trajectory

The planar viffing trajectory is generated by a sequence of waypoints defining 180° lateral turning points in a single vertical plane based on iterative estimates of plume source location (Fig. 5a). The waypoints are distributed on both sides of the target following a planar decaying oscillation in the vertical plane that converges to the plume source. The penetrator must estimate the plume source location from its current location within the plume and determine the remaining waypoints to the plume source. According to Russell et al. (2003), both the search area and the number of maneuvers affect the accuracy of source localization. A larger search area provides global information about the plume while number of maneuvers provides local information. We define $FE$ as the fuel efficiency for plume mapping given by

$$FE = \begin{cases} \frac{LN}{\Delta V} & \text{for planar viffing} \\ \frac{DN}{\Delta V} & \text{for boxes viffing and quasi} - \text{spiral} \end{cases}$$

where $N$ is the number of maneuvers, and $L$ and $D$ are the largest searching distance for planar viffing and the largest area for boxes viffing and quasi-spiral viffing respectively

Planar viffing enables the penetrator to explore the plume in a vertical plane with the largest lateral distance initially of 90 km decreasing with altitude. Compared with the ballistic trajectory, planar viffing requires more fuel because of the large lateral maneuvers. However, the search area, and most importantly, the number of measured data points, is expanded by these maneuvers which improves the accuracy of plume mapping and source localization. Simulation results (Table 5) indicate that planar viffing's fuel consumption and fuel efficiency ($FE = 0.738$) are both modest compared with other viffing strategies. However, the plume data in the cross sections outside the viffing plane are still under-sampled compared with the trajectory of nested boxes suggesting that localization accuracy may be more limited.

### 4.3. Viffing trajectory of nested boxes

To sample the area outside a single viffing plane, we set a sequence of waypoints scattered around the plume source through all vertical planes which we refer to as a 'box tra-
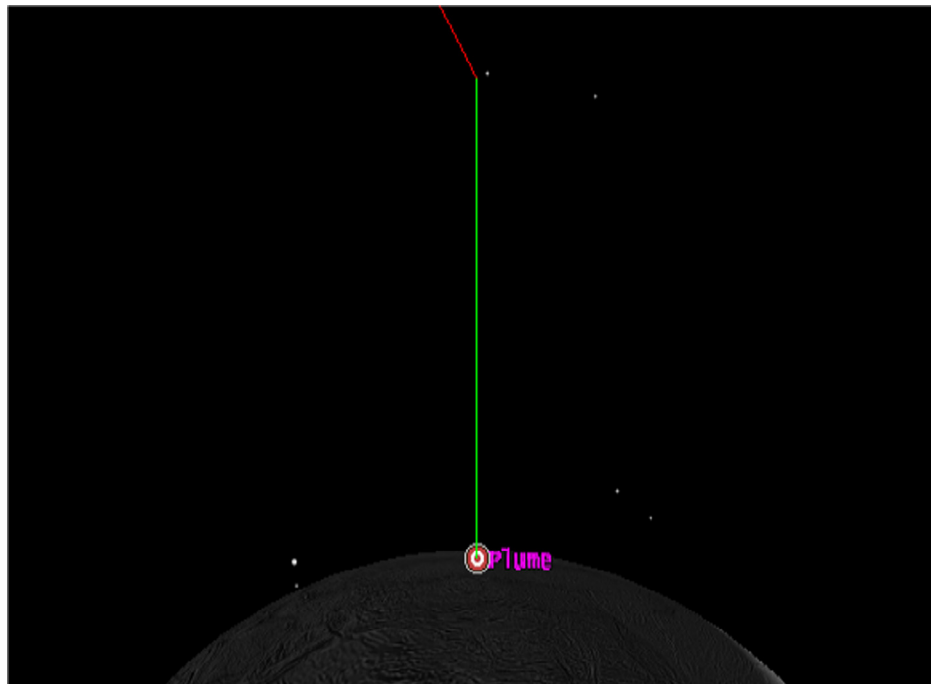
Fig. 4. Simulation of the ballistic trajectory (green line). We assume that the plume source is located at Enceladus' south pole with the release point of the penetrator located directly above the source. (For interpretation of the references to colour in this figure legend, the reader is referred to the web version of this article.)

Table 4
Maneuver summary of the ballistic trajectory with time, mission segments, $\Delta V$ costs of each maneuver and fuel consumptions with mission segments including interplanetary maneouvre, targeting the sphere of influence (SOI) and the descent itself.

| Time | Segment | $\Delta V$ (m s$^{-1}$) | Fuel Used (kg) |
|---|---|---|---|
| 00:00:00.000 | Interplanetary | 27.89 | 0.12 |
| 12:27:39.759 | Target SOI | 153.50 | 0.66 |
| 13:20:31.399 | Impact Control | 66.98 | 0.28 |
| | Summary | 248.38 | 1.06 |

jectory' since it forms a series of nested boxes (Fig. 6a). By performing a 'box trajectory', the penetrator searches the plume with an initial largest lateral search radius of 90 km subsequently decreasing with altitude. Simulation results of the 'box trajectory' (Table 6) illustrate the 360° search excursion which extends the search area. Thus, the accuracy of plume mapping and the fuel efficiency (*FE* = 21.9) are both improved.
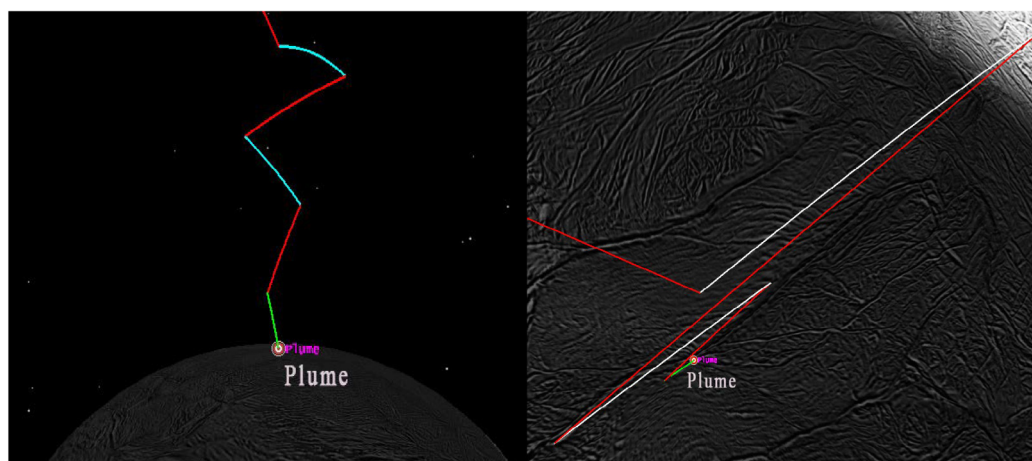


(a) Planar viffing trajectory, side view          (b) Planar viffing trajectory, vertical view
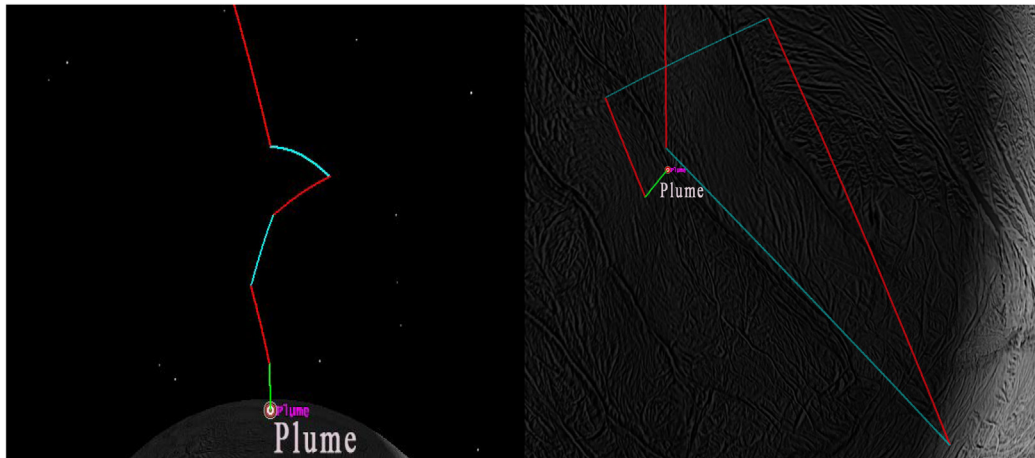
Fig. 5. Planar viffing trajectory with 6 waypoints within the plume. (a) side view and (b) vertical view. Trajectory segments are distinguished by different colours. (For interpretation of the references to colour in this figure legend, the reader is referred to the web version of this article.)

Table 5
Maneuver summary of planar viffing including duration from release, waypoint positions and altitudes, penetrator velocity at the waypoints, $\Delta V$ costs and fuel consumption. The waypoint positions and velocities are referred to inertial coordinates.

| Duration Time (s) | Waypoints Position (km) | Waypoints Velocity (m s$^{-1}$) | Altitude (km) | $\Delta V$ (m s$^{-1}$) | Fuel Used (kg) |
|---|---|---|---|---|---|
| 0 | (60,0,−434) | (−130,0,40) | 190 | 54.84 | 0.28 |
| 1117 | (−30,0,−397) | (80,0,70) | 150 | 182.41 | 0.91 |
| 1812 | (20,0,−347) | (80,0,100) | 100 | 214.99 | 1 |
| 2400 | (−10,0,−288) | (40,0,140) | 40 | 142.75 | 0.63 |
| 2915 | (0,0,−249) | (0,0,161) | 1 | 96.61 | 0.41 |
| 3171 | (0,0,−248) | (0,0,162) | 0 | 38.31 | 0.16 |
| Summary | | | | 729.92 | 3.38 |



(a) 'Box trajectory', side view      (b) 'Box trajectory', vertical view

Fig. 6. 'Box trajectory' of 6 waypoints above the plume area of Enceladus including (a) side view and (b) vertical view. Trajectory segments are distinguished by different colours. (For interpretation of the references to colour in this figure legend, the reader is referred to the web version of this article.)

Table 6
Maneuver summary of 'box trajectory' including duration from release, waypoint positions and altitudes, penetrator velocity at waypoints, $\Delta V$ costs and fuel consumption. The waypoint positions and velocities are with respect to inertial coordinates.

| Duration Time (s) | Waypoints Position (km) | Waypoints Velocity (m s$^{-1}$) | Altitude (km) | $\Delta V$ (m s$^{-1}$) | Fuel Used (kg) |
|---|---|---|---|---|---|
| 0 | (60,0,−434) | (−100,−400,40) | 190 | 54.85 | 0.26 |
| 1117 | (0,−30,−397) | (0,50,700) | 150 | 144.91 | 0.67 |
| 1813 | (−20, 0,−347) | (40,20,100) | 100 | 107.25 | 0.48 |
| 2411 | (0, 10,−288) | (0,40,140) | 40 | 78.55 | 0.34 |
| 2910 | (0,0,−249.33) | (0,0,161) | 1 | 69.21 | 0.289 |
| 3171 | (0,0,−248) | (0,0,162) | 0 | 38.29 | 0.16 |
| Summary | | | | 493.05 | 2.19 |

## 4.4. Quasi-spiral trajectory

We have adopted biomimetic search strategies based on animal behaviours that track ambient signals (Pyk et al., 2006; L. et al., 2011; Gonzalez et al., 2004). Moths tend to fly to any light source at night (phototaxis) for which several hypotheses have been proposed (Wang, 2018). The most favoured theory is that moths fly with a 90° path angle to any "celestial" light source which is appropriate to the Sun and Moon under natural conditions but this results in a logarithmic spiral trajectory around any point source of light at night. The logarithmic spiral be

it an equiangular spiral or a growth spiral is defined in polar coordinates by:

$$r = ae^{b\theta}, \tag{9}$$

as shown in Fig. 7a, or in a parametric form by,

$$x(t) = r(t)\cos(t) = ae^{bt}\cos(t),$$
$$y(t) = r(t)\sin(t) = ae^{bt}\sin(t) \tag{10}$$

where $a$ and $b$ are both real numbers. The distance between the turning points decreases in geometric progression in a logarithmic spiral. Fig. 7b shows a schematic trajectory

(a) Spiral trajectory, vertical view
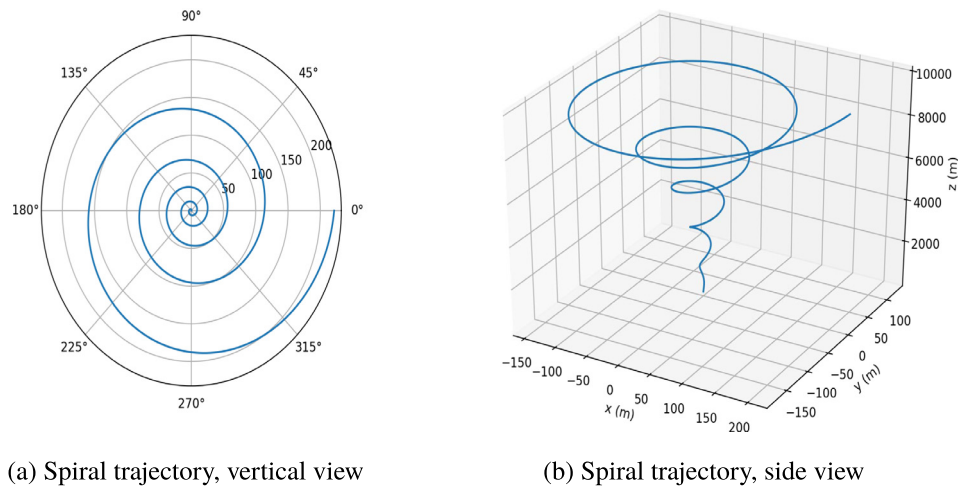
(b) Spiral trajectory, side view

Fig. 7. Spiral descent profile: (a) vertical view in polar coordinates, and (b) side view in cartesian coordinates.

with a logarithmic spiral laterally with a longitudinal free fall.

In Enceladus plume mapping, the lateral logarithmic spiral trajectory achieves a 360° search area with a geometric convergence. Such a trajectory can be generated through a trajectory tracking algorithm. An onboard computer first generates a reference trajectory above the estimated source given by a spiral function, then it enforces control of the penetrator to track the spiral. However, trajectory tracking imposes high $\Delta V$ to be accurate. Also, the velocity vector on a logarithmic spiral trajectory is constantly changing, implying a continuously consuming of propellant.

We propose a quasi-spiral trajectory to compromise between the $\Delta V$ costs and trajectory approximation accuracy by choosing a sequence of arbitrary waypoints on the spiral trajectory, shown in Fig. 8 and Table 7. The accuracy of approximation can be improved by increasing number of waypoints with the incumbent extra costs of fuel consumption. The fuel efficiency for plume mapping of the
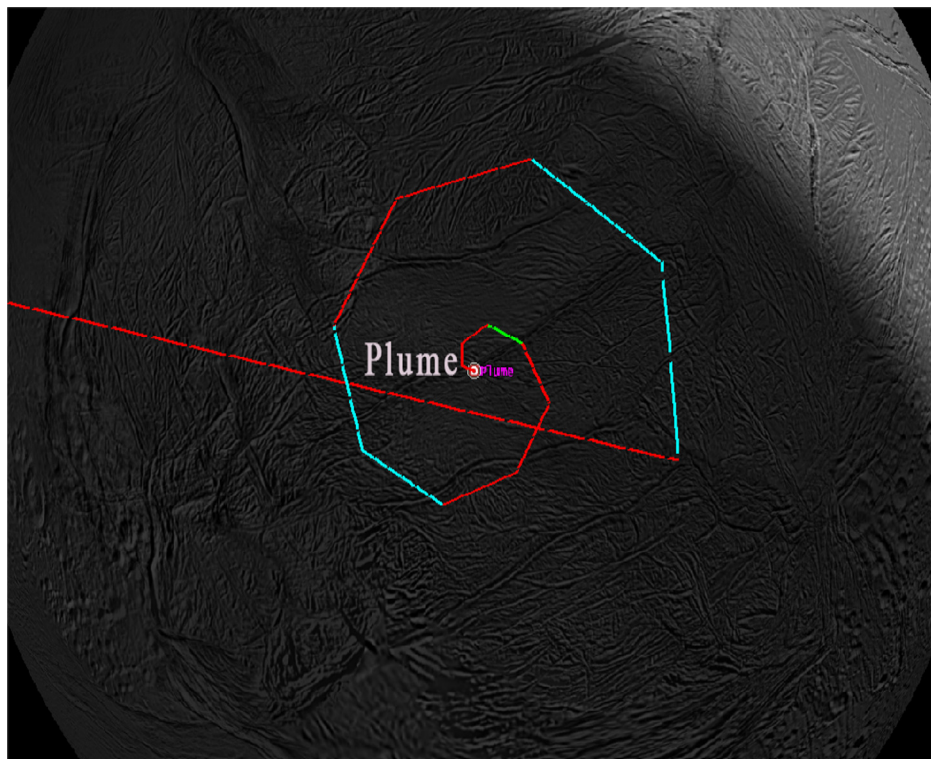


Fig. 8. Quasi-spiral trajectory above the plume area of Enceladus. Trajectory segments are distinguished by different colours. (For interpretation of the references to colour in this figure legend, the reader is referred to the web version of this article.)

Table 7
Maneuver summary of quasi-spiral trajectory with duration from release, waypoint positions and altitudes, penetrator velocity at waypoints, $\Delta V$ costs and fuel consumption. The waypoint positions and velocities are referred to inertial coordinates.

| Duration Time (s) | Waypoints Positon (km) | Waypoints Velocity (m s$^{-1}$) | Altitude (km) | $\Delta V$ (m s$^{-1}$) | Fuel Used (kg) |
|---|---|---|---|---|---|
| 0 | (60,0,−450.4) | (−49,−93,19.6) | 206 | 81.76 | 0.50 |
| 561 | (39,−39,−439) | (−105,−30,34) | 194 | 81.19 | 0.48 |
| 980 | (0,−50,−423.4) | (−101.6,56,49) | 178 | 82.67 | 0.48 |
| 1350 | (−32,−32,−406) | (−31.5,124,62) | 160 | 85.58 | 0.48 |
| 1666 | (−40,0,−388) | (67,113,74) | 142 | 96.39 | 0.53 |
| 1922 | (−25,25,−371) | (97,20,85) | 124 | 98.51 | 0.52 |
| 2143 | (0,30,−347) | (119,−79,99) | 100 | 97.22 | 0.49 |
| 2400 | (18,18,−331) | (11,−92,109) | 84 | 100.49 | 0.49 |
| 2551 | (20,0,−309) | (−76,−86,122) | 61 | 109.15 | 0.52 |
| 2747 | (10,−10,−292) | (−91,5.6,132) | 45 | 85.72 | 0.39 |
| 2871 | (0,−10,−277) | (−33,59.5,142) | 29 | 92.47 | 0.41 |
| 2986 | (−4,−4,−261) | (43,43,152) | 13 | 78.95 | 0.34 |
| 3094 | (−1,−1,−251) | (43,43,159) | 0.1 | 77.78 | 0.33 |
| 3171 | (0,0,−248) | (0,0,162) | 0 | 60.52 | 0.25 |
| Summary | | | | 1228.40 | 6.22 |

Table 8
Maneuver summary of all types of viffing including free fall impact and 300 m/s impact with maneuver types, impact velocities, number of waypoints, $\Delta V$ costs, fuel consumption and fuel efficiencies.

| Types | Impact Velocity (m s$^{-1}$) | Waypoint Number | $\Delta V$ (m s$^{-1}$) | Fuel Used (kg) | Fuel Efficiency |
|---|---|---|---|---|---|
| Ballistic | 162 m/s | 0 | 69.04 | 0.29 | 0 |
| Ballistic | 300 m/s | 0 | 279.15 | 1.19 | 0 |
| Planar | 162 m/s | 6 | 723.23 | 3.34 | 0.7 |
| Planar | 162 m/s | 3 | 326.97 | 1.41 | 0.8 |
| Planar | 300 m/s | 6 | 861.89 | 4.08 | 0.6 |
| Planar | 300 m/s | 3 | 465.17 | 1.96 | 0.5 |
| Boxing | 162 m/s | 6 | 487.83 | 2.16 | 22.1 |
| Boxing | 162 m/s | 3 | 277.5 | 1.19 | 19.4 |
| Boxing | 300 m/s | 6 | 631.35 | 2.87 | 17.1 |
| Boxing | 300 m/s | 3 | 415.99 | 2.873 | 13 |
| Spiral | 162 m/s | 14 | 1228.4 | 5.72 | 128.8 |
| Spiral | 300 m/s | 14 | 1365.56 | 7.09 | 115.8 |

proposed quasi-spiral viffing is $FE = 128.94$ which is the highest among all the viffing options.

The result in Table 7 indicate that the quasi-spiral trajectory imposes the one of the highest $\Delta V$ costs but it samples the largest plume data set implying the smallest source localization error among all the viffing strategies. By performing a quasi-spiral trajectory, the penetrator is able to search a conical area whose vertex is the plume source with the largest search radius of 90 km that subsequently diminishes.

All types of viffing trajectories are summarized in Table 8 with an impact velocity of both 162 m s$^{-1}$ (free fall) and 300 m s$^{-1}$ (higher end of the terminal velocity constraint achieved through additional vertical thrust during descent) demonstrating that the quasi-spiral with free fall achieves the highest fuel efficiency for plume mapping.

## 5. Discussion

We have analysed the problem of targeting sources of water vapour plumes on Enceladus in the context of a life detection mission. We simulated four different descent pro-

files that permit the plume to be mapped during the descent in order to pinpoint desirable landing sites (nominally at the plume vents). The simulation results suggest that the quasi-spiral trajectory has the advantage of fuel efficiency while offering the largest search area for plume measurements and effective targeting.

We are pursuing several developments that may enhance the concept including optimization of the waypoints and methods of SLIM.

### 5.1. Optimization of waypoints sequence

The positions of the waypoints have a great influence on fuel consumption. Thus, fuel consumption could be conserved by optimizing the waypoint sequence. Maneuver velocity $v_{i,i+1}$ between waypoint $(x_i, y_i, z_i)$ and $(x_{i+1}, y_{i+1}, z_{i+1})$ is given by:

$$v_{i,i+1} = \frac{s_{i,i+1}}{t_{i,i+1}} \qquad (11)$$

where $s_{i,i+1} = \sqrt{(x_i - x_{i-1})^2 + (y_i - y_{i-1})^2}$. Note that time $t_{i,i+1}$ is governed by longitudinal motion in Algorithm 1. Because the maneuver $\Delta V_i$ at waypoint $(x_{i+1}, y_{i+1})$ is $v_{i+1,i+2} - v_{i,i+1}$, solves the optimal sequence of waypoints for minimal $\Delta V$ constrained by a reference trajectory function $f(x_i, y_i)$ modelling any viffing strategy. This optimization problem has yet to be solved.

**Problem 1.**

$$\min \quad \sum_0^n \frac{s_{i,i+1}}{t_{i,i+1}}$$

$$\text{s.t.} \quad s_{i,i+1} = \sqrt{(x_i - x_{i-1})^2 + (y_i - y_{i-1})^2},$$

$$f(x_i, y_i) = 0.$$

### 5.2. Source likelihood map algorithm

SLIM methods using the data accumulated by viffing maneuvers becomes the most crucial problem for the proposed mission conception. There have been studies in 2D plume mapping techniques using wheeled robot on the ground, but 3D plume mapping methods using spacecraft such as penetrators have not been addressed to our knowledge. In 2D scenarios, the commonest methods are biologically inspired behaviour-based approaches including gradient-based strategies (Grasso et al., 2000) and infotaxis strategies (Vergassola et al., 2007). We are investigating methods for estimating the source location using a hidden Markov model with sequential Monte Carlo (SMC) techniques (Farrell et al., 2003; Li et al., 2011). Unfortunately, the time computational complexity of SMC is still an obstacle for online mapping using spacecraft onboard computers. Notwithstanding that, plume source separation - the identification of a single source from mixed plume signals from multiple plume sources - is another unsolved problem because the material from multiple jets are mixed together.

Finally, active attitude control of the 6-DOF dynamics of a penetrator during descent has not been addressed but is a necessary component of the descent and landing system.

### 5.3. Applications for other planetary missions

Planetary penetrator missions that permit in-situ exploration of a descent volume around the target area and flexibly determine the impact site autonomously may also be attractive for other planetary missions. On the rich organic chemistry world of Titan (Coates et al., 2007), the use of one or more penetrators would greatly enhance the scientific returns for a landing mission by providing a means to measure the atmospheric chemistry and locate specific sites of interest identified during the descent. Similar to Enceladus, water plumes from the icy crust of Europa (Jia et al., 2018), down to depths of ¸1 cm to 20 cm

(Nordheim et al., 2018) represent another possible site for penetrator missions that may be used for bio-signature targeting. The proposed lateral maneuver profiles may also be applicable to sample acquisition missions on comets or asteroids surveying and targeting the surface for targets of interest (Völk et al., 2018).

## 6. Conclusion

In order to investigate the potential astrobiological environment of Enceladus, we propose a method that impacts into the ice crust at plume vents with penetrators employing a biomimetic plume sniffing approach. We believe that this approach, although discussed in terms of a penetrator mission, is directly applicable to any life detection mission to Enceladus. By penetrating the ice crust and deploy the scientific instruments into it directly, the proposed method also offers the greatest chance of accessing pristine samples from the subsurface ocean for astrobiological investigation. In addition, the biomimetic plume sniffing method enables the penetrator to map the plume and locate its source autonomously during the descent, even when the prior knowledge of the source location is insufficient. This provides the prospect of developing autonomous landing systems where the landing target is unknown before the descent phase.

**Appendix A.** The 6 degrees of freedom dynamic equations of a penetrator is given by Eq. (12) 6-DOF dynamic equations of a penetrator is given by:

$$m\frac{dV}{dt} = P\cos\alpha\cos\beta + \frac{T_d}{\pi}\sin\dot{\gamma}t_c(K_{dz}\sin\beta - K_{dy}\sin\alpha\cos\beta)$$

$$mV\frac{d\theta}{dt} = P\sin\alpha - mg + \frac{T_d}{\pi}\sin\dot{\gamma}t_c K_{dy}\cos\alpha$$

$$-mV\frac{d\psi_V}{dt} = P\cos\alpha\sin\beta + \frac{T_d}{\pi}\sin\dot{\gamma}t_c K_{dy}\sin\alpha\sin\beta - K_{dz}cos\beta$$

$$\frac{dx}{dt} = V\cos\psi_V$$

$$\frac{dy}{dt} = V\sin\theta$$

$$\frac{dz}{dt} = -V\sin\psi_V$$

$$J_x\frac{d\omega_x}{dt} = -(J_z - J_y)\omega_z\omega_y$$

$$J_y\frac{d\omega_y}{dt} = \frac{T_a}{\pi}\sin(\gamma_c + \dot{\gamma}t_c)\sin(\dot{\gamma}t_c)(x_F - x_G) - (J_x - J_z)\omega_x\omega_z$$
$$+ J_z\omega_z\dot{\gamma}$$

$$J_z\frac{d\omega_z}{dt} = -\frac{T_a}{\pi}\cos(\gamma_c + \dot{\gamma}t_c)\sin(\dot{\gamma}t_c)(x_F - x_G) - (J_y - J_x)\omega_y\omega_z$$
$$+ J_y\omega_y\dot{\gamma}$$

$$\frac{d\gamma}{dt} = \omega_x - \omega_y\tan\vartheta$$

$$\frac{d\psi}{dt} = \frac{1}{\cos\vartheta}\omega_y$$

$$\frac{d\vartheta}{dt} = \omega_z$$

$$\frac{dm}{dt} = m_c$$

$$(12)$$

Here, $V$ = velocity, $\theta$ = flight path angle, $\psi_V$ = flight path azimuth angle, $(\alpha, \beta, \gamma_V)$ = trajectory angles in velocity system, $(x, y, z)$ = inertial coordinates, $(\gamma, \psi, \vartheta)$ = attitude angles, $(\omega_x, \omega_y, \omega_z)$ = angular velocities vector, $(J_x, J_y, J_z)$

= moment of inertia, $P$ = main thrust, $T_d$ = control thrust, $T_a$ = control torque, $t_c$ = roll period, $x_G$ = distance from the nose to centre of mass, $x_F$ = distance from nose to centre of force, $m$ = mass, $K_y = \sin(\gamma_c + \dot{\gamma} t_c)$ and $K_z = -\cos(\gamma_c + \dot{\gamma} t_c)$. The first 6 equations of Eq. (12) govern the trajectory dynamics with a periodic control force $T_d$ being coupled with rolling motion; 7th - 12th equations represent the attitude dynamics controlled by $T_a$ via $\frac{T_a}{\pi} \sin(\dot{\gamma} t_c)(x_F - x_G)$. The last equation denotes the dynamic of mass consumption due to propellant burning. The penetrator controls its attitude and trajectory using a pair of thrusters based on the dynamic equations ($T_d = T_c$), which simplifies the model. However, the rolling motion not only introduces a complex nonlinear segment into the dynamics but it also imposes coupling between the attitude control loop with the trajectory control loop, rendering complications to the design of the control system. It is also difficult to maneuver laterally during the flight due to the gyroscopic stiffness imparted by the spin. Therefore, one or more thrusters are required ($T_d \neq T_c$) to decouple the attitude dynamics from the trajectory dynamics and permit the ability to turn in mid-flight. (Gao et al., 2007).

## References

Allwood, A.C., Rosing, M.T., Flannery, D.T., Hurowitz, J.A., Heirwegh, C.M., 2018. Reassessing evidence of life in 3,700-million-year-old rocks of Greenland. Nature 563, 241–244. https://doi.org/10.1038/s41586-018-0610-4.

Anderson, W.W., Ahrens, T.J., Gibson, A., Scott, R., Suzuki, K., 1996. Emplacement of penetrators into planetary surfaces. J. Geophys. Res.: Planets 101, 21137–21149. https://doi.org/10.1029/96je01421.

Barge, L.M., White, L.M., 2017. Experimentally testing hydrothermal vent origin of life on Enceladus and other icy/ocean worlds. Astrobiology 17, 820–833. https://doi.org/10.1089/ast.2016.1633.

Coates, A.J., Crary, F.J., Lewis, G.R., Young, D.T., Waite, J.H., Sittler, E.C., 2007. Discovery of heavy negative ions in Titan's ionosphere. Geophys. Res. Lett. 34. https://doi.org/10.1029/2007gl030978.

Coustenis, A., Atreya, S.K., Balint, T., Brown, R.H., Dougherty, M.K., Ferri, F., Fulchignoni, M., Gautier, D., Gowen, R.A., Griffith, C.A., Gurvits, L.I., Jaumann, R., Langevin, Y., Leese, M.R., Lunine, J.I., McKay, C.P., Moussas, X., Müller-Wodarg, I., Neubauer, F., Owen, T.C., Raulin, F., Sittler, E.C., Sohl, F., Sotin, C., Tobie, G., Tokano, T., Turtle, E.P., Wahlund, J.E., Waite, J.H., Baines, K.H., Blamont, J., Coates, A.J., Dandouras, I., Krimigis, T., Lellouch, E., Lorenz, R.D., Morse, A., Porco, C.C., Hirtzig, M., Saur, J., Spilker, T., Zarnecki, J.C., Choi, E., Achilleos, N., Amils, R., Annan, P., Atkinson, D.H., Bénilan, Y., Bertucci, C., Bézard, B., Bjoraker, G.L., Blanc, M., Boireau, L., Bouman, J., Cabane, M., Capria, M.T., Chassefière, E., Coll, P., Combes, M., Cooper, J.F., Coradini, A., Crary, F., Cravens, T., Daglis, I.A., de Angelis, E., de Bergh, C., de Pater, I., Dunford, C., Durry, G., Dutuit, O., Fairbrother, D., Flasar, F.M., Fortes, A.D., Frampton, R., Fujimoto, M., Galand, M., Grasset, O., Grott, M., Haltigin, T., Herique, A., Hersant, F., Hussmann, H., Ip, W., Johnson, R., Kallio, E., Kempf, S., Knapmeyer, M., Kofman, W., Koop, R., Kostiuk, T., Krupp, N., Küppers, M., Lammer, H., Lara, L.M., Lavvas, P., Le Mouélic, S., Lebonnois, S., Ledvina, S., Li, J., Livengood, T.A., Lopes, R.M., Lopez-Moreno, J.J., Luz, D., Mahaffy, P.R., Mall, U., Martinez-Frias, J., Marty, B., McCord, T., Menor Salvan, C., Milillo, A., Mitchell, D.G., Modolo, R., Mousis, O., Nakamura, M., Neish, C.D., Nixon, C.A., Nna Mvondo, D., Orton, G., Paetzold, M., Pitman, J., Pogrebenko, S., Pollard, W., Prieto-Ballesteros, O., Rannou, P., Reh, K., Richter, L., Robb, F.T.,

Rodrigo, R., Rodriguez, S., Romani, P., Ruiz Bermejo, M., Sarris, E.T., Schenk, P., Schmitt, B., Schmitz, N., Schulze-Makuch, D., Schwingenschuh, K., Selig, A., Sicardy, B., Soderblom, L., Spilker, L.J., Stam, D., Steele, A., Stephan, K., Strobel, D.F., Szego, K., Szopa, C., Thissen, R., Tomasko, M.G., Toublanc, D., Vali, H., Vardavas, I., Vuitton, V., West, R.A., Yelle, R., Young, E.F., 2009. TandEM: Titan and Enceladus mission. Exp. Astron. 23, 893–946. https://doi.org/10.1007/s10686-008-9103-z.

Dodd, M.S., Papineau, D., Grenne, T., Slack, J.F., Rittner, M., Pirajno, F., O'Neil, J., Little, C.T.S., 2017. Evidence for early life in Earth's oldest hydrothermal vent precipitates. Nature 543, 60–64. https://doi.org/10.1038/nature21377.

Domagal-Goldman, S.D., Wright, K.E., Adamala, K., Arina de la Rubia, L., Bond, J., Dartnell, L.R., Goldman, A.D., Lynch, K., Naud, M.E., Paulino-Lima, I.G., Singer, K., Walter-Antonio, M., Abrevaya, X.C., Anderson, R., Arney, G., Atri, D., Azúa-Bustos, A., Bowman, J.S., Brazelton, W.J., Brennecka, G.A., Carns, R., Chopra, A., Colangelo-Lillis, J., Crockett, C.J., DeMarines, J., Frank, E.A., Frantz, C., de la Fuente, E., Galante, D., Glass, J., Gleeson, D., Glein, C.R., Goldblatt, C., Horak, R., Horodyskyj, L., Kaçar, B., Kereszturi, A., Knowles, E., Mayeur, P., McGlynn, S., Miguel, Y., Montgomery, M., Neish, C., Noack, L., Rugheimer, S., Stüeken, E.E., Tamez-Hidalgo, P., Walker, S.I., Wong, T., 2016. The astrobiology primer v2.0. Astrobiology 16, 561–653. https://doi.org/10.1089/ast.2015.1460.

Farrell, J., Pang, Shuo, Li, Wei, 2003. Plume mapping via hidden markov methods. IEEE Trans. Syst. Man Cybernet. Part B (Cybernet.) 33, 850–863. https://doi.org/10.1109/tsmcb.2003.810873.

Flamm, J., Deere, K., Mason, M., Berrier, B., Johnson, S., 2007. Experimental study of an axisymmetric dual throat fluidic thrust vectoring nozzle for supersonic aircraft application. In: 43rd AIAA/ASME/SAE/ASEE Joint Propulsion Conference & Exhibit. American Institute of Aeronautics and Astronautics, Cincinnati, OH. https://doi.org/10.2514/6.2007-5084.

Gal-Or, B., 1990. Vectored aircraft and supermaneuverability. In: Vectored Propulsion, Supermaneuverability and Robot Aircraft. Springer New York, New York, NY, pp. 78–104. https://doi.org/10.1007/978-1-4613-8961-3_6.

Gao, Yang, Ellery, A., Jaddou, M., Vincent, J., Eckersley, S., 2007. Planetary micro-penetrator concept study with biomimetic drill and sampler design. IEEE Trans. Aerosp. Electron. Syst. 43, 875–885. https://doi.org/10.1109/taes.2007.4383580.

Geissler, P., 2015. Cryovolcanism in the outer solar system. In: The Encyclopedia of Volcanoes. Elsevier, pp. 763–776. https://doi.org/10.1016/B978-0-12-385938-9.00044-4.

German, C.R., 2004. Hydrothermal exploration and astrobiology: oases for life in distant oceans? Int. J. Astrobiol. 3, 81–95. https://doi.org/10.1017/s1473550404002009.

Gilichinsky, D., Vorobyova, E., Erokhina, L., Fyordorov-Dayvdov, D., Chaikovskaya, N., 1992. Long-term preservation of microbial ecosystems in permafrost. Adv. Space Res. 12, 255–263. https://doi.org/10.1016/0273-1177(92)90180-6.

Góbi, S., Kereszturi, Á., 2017. Role of serpentinization in the thermal and connected mineral evolution of planetesimals – evaluating possible consequences for exoplanetary systems. Mon. Not. R. Astron. Soc. 466, 2099–2110. https://doi.org/10.1093/mnras/stw3223.

Gonzalez, E., Mascenon, F., Magpantay, A., Go, K., Cordero, M., 2004. Design of an autonomous mobile olfactory robot for chemical source localization. In: 2004 IEEE Region 10 Conference TENCON 2004, IEEE, Chiang Mai, Thailand. pp. 475–478. doi:https://doi.org/10.1109/TENCON.2004.1414973.

Gowen, R., Smith, A., Fortes, A., Barber, S., Brown, P., Church, P., Collinson, G., Coates, A., Collins, G., Crawford, I., Dehant, V., Chela-Flores, J., Griffiths, A., Grindrod, P., Gurvits, L., Hagermann, A., Hussmann, H., Jaumann, R., Jones, A., Joy, K., Karatekin, O., Miljkovic, K., Palomba, E., Pike, W., Prieto-Ballesteros, O., Raulin, F., Sephton, M., Sheridan, S., Sims, M., Storrie-Lombardi, M., Ambrosi, R., Fielding, J., Fraser, G., Gao, Y., Jones, G., Kargl, G., Karl, W., Macagnano, A., Mukherjee, A., Muller, J., Phipps, A.,

Pullan, Richter, L., Sohl, F., Snape, J., Sykes, J., Wells, N., 1997. Penetrators for in situ subsurface investigations of Europa. Adv. Space Res. 48, 725–742. https://doi.org/10.1016/j.asr.2010.06.026.

Grasso, F.W., Consi, T.R., Mountain, D.C., Atema, J., 2000. Biomimetic robot lobster performs chemo-orientation in turbulence using a pair of spatially separated sensors: progress and challenges. Robot. Autonomous Syst. 30, 115–131. https://doi.org/10.1016/s0921-8890(99)00068-8.

Grygorczuk, J., Banaszkiewicz, M., Cichocki, A., Ciesielska, M., Dobrowolski, M., Krasowski, J., Kuci, T., Skocki, K., Spohn, T., Szewczyk, T., Wawrzaszek, R., Wi, Ł., 2011. Advanced penetrators and hammering sampling devices for planetary. Body Explor., 8

Hansen, C.J., 2006. Enceladus' water vapor plume. Science 311, 1422–1425. https://doi.org/10.1126/science.1121254.

Hargitai, H., Kereszturi, 2015. Encyclopedia of Planetary Landforms, first ed. Springer-Verlag, New York.

Ikaza, D., 2000. Thrust Vectoring Nozzle for. Modern Military Aircraft.

Jia, X., Kivelson, M.G., Khurana, K.K., Kurth, W.S., 2018. Evidence of a plume on Europa from Galileo magnetic and plasma wave signatures. Nat. Astronomy 2, 459–464. https://doi.org/10.1038/s41550-018-0450-z.

Jost, B., Thomas, N., Pommerol, A., Poch, O., Cerubini, R., Yoldi, Z., 2018. Experimental characterization of fine-grained water ice particles: evolution of photometric and polarimetric phase curves due to grain sintering. Applications to plume depositions on icy satellites. In: 42nd COSPAR Scientific Assembly, pp. B5.3–45–18.

Kereszturi, Á., 2018. Evaluation of instruments for coming europa missions to conduct research on astrobiology. In: 49th Lunar and Planetary Science Conference, The Woodlands, Texas.

Kereszturi, A., Keszthelyi, Z., 2013. Astrobiological implications of chaos terrains on Europa to help targeting future missions. Planet. Space Sci. 77, 74–90. https://doi.org/10.1016/j.pss.2012.08.028.

Konstantinidis, K., Flores Martinez, C.L., Dachwald, B., Ohndorf, A., Dykta, P., Bowitz, P., Rudolph, M., Digel, I., Kowalski, J., Voigt, K., Förstner, R., 2015. A lander mission to probe subglacial water on Saturn's moon Enceladus for life. Acta Astronaut. 106, 63–89. https://doi.org/10.1016/j.actaastro.2014.09.012.

Krupp, N., Roussos, E., Kollmann, P., Paranicas, C., Mitchell, D., Krimigis, S., Rymer, A., Jones, G., Arridge, C., Armstrong, T., Khurana, K., 2012. The Cassini Enceladus encounters 2005–2010 in the view of energetic electron measurements. Icarus 218, 433–447. https://doi.org/10.1016/j.icarus.2011.12.018.

L., L., Vouloutsi, V., Escuredo, A., Marcos, E., i Badia, S.B., Mathews, Z., F.M.J., P., Ziyatdinov, A., i Llu, A.P., 2011. Moth-like chemo-source localization and classification on an indoor autonomous robot. In: Pramatarova, L. (Ed.), On Biomimetics. InTech, pp. 454–463. doi:10.5772/19695.

Li, J.G., Meng, Q.H., Wang, Y., Zeng, M., 2011. Odor source localization using a mobile robot in outdoor airflow environments with a particle filter algorithm. Autonomous Robots 30, 281–292. https://doi.org/10.1007/s10514-011-9219-2.

Lorenz, R.D., 2011. Planetary penetrators: their origins, history and future. Adv. Space Res. 48, 403–431. https://doi.org/10.1016/j.asr.2011.03.033.

McKay, C.P., 2008. An approach to searching for life on Mars, Europa, and Enceladus. Space Sci. Rev. 135, 49–54. https://doi.org/10.1007/s11214-007-9229-8.

Nordheim, T.A., Hand, K.P., Paranicas, C., 2018. Preservation of potential biosignatures in the shallow subsurface of Europa. Nat. Astronomy 2, 673–679. https://doi.org/10.1038/s41550-018-0499-8.

Porco, C.C., 2006. Cassini observes the active south pole of Enceladus. Science 311, 1393–1401. https://doi.org/10.1126/science.1123013.

Porco, C.C., Dones, L., Mitchell, C., 2017. Could it be snowing microbes on Enceladus? Assessing conditions in its plume and implications for future missions. Astrobiology 17, 876–901. https://doi.org/10.1089/ast.2017.1665.

Postberg, F., Schmidt, J., Hillier, J., Kempf, S., Srama, R., 2011. A saltwater reservoir as the source of a compositionally stratified plume on Enceladus. Nature 474, 620–622. https://doi.org/10.1038/nature10175.

Postberg, F., Khawaja, N., Abel, B., Choblet, G., Glein, C.R., Gudipati, M.S., Henderson, B.L., Hsu, H.W., Kempf, S., Klenner, F., Moragas-Klostermeyer, G., Magee, B., Nölle, L., Perry, M., Reviol, R., Schmidt, J., Srama, R., Stolz, F., Tobie, G., Trieloff, M., Waite, J.H., 2018. Macromolecular organic compounds from the depths of Enceladus. Nature 558, 564–568. https://doi.org/10.1038/s41586-018-0246-4.

Pyk, P., Bermúdez i Badia, S., Bernardet, U., Knüsel, P., Carlsson, M., Gu, J., Chanie, E., Hansson, B.S., Pearce, T.C., J. Verschure, P.F.M., 2006. An artificial moth: chemical source localization using a robot based neuronal model of moth optomotor anemotactic search. Autonomous Robots 20, 197–213. https://doi.org/10.1007/s10514-006-7101-4.

Raus, R., Gao, Y., Wu, Y., Watt, M., 2012. Analysis of state-of-the-art single-thruster attitude control techniques for spinning penetrator. Acta Astronaut. 76, 60–78. https://doi.org/10.1016/j.actaastro.2012.02.014.

Russell, R., Bab-Hadiashar, A., Shepherd, R.L., Wallace, G.G., 2003. A comparison of reactive robot chemotaxis algorithms. Robot. Autonomous Syst. 45, 83–97. https://doi.org/10.1016/s0921-8890(03)00120-9.

Saur, J., Schilling, N., Neubauer, F.M., Strobel, D.F., Simon, S., Dougherty, M.K., Russell, C.T., Pappalardo, R.T., 2008. Evidence for temporal variability of Enceladus' gas jets: modeling of Cassini observations. Geophys. Res. Lett. 35. https://doi.org/10.1029/2008gl035811.

Vance, S., Harnmeijer, J., Kimura, J., Hussmann, H., deMartin, B., Brown, J.M., 2007. Hydrothermal systems in small ocean planets. Astrobiology 7, 987–1005. https://doi.org/10.1089/ast.2007.0075.

Vergassola, M., Villermaux, E., Shraiman, B.I., 2007. 'Infotaxis' as a strategy for searching without gradients. Nature 445, 406–409. https://doi.org/10.1038/nature05464.

Völk, S., Ulamec, S., Biele, J., Hecht, M., Lell, P., Fleischmann, J., Althapp, S., Grebenstein, M., Nuth, J.A., Wegel, D.C., Smith, W.F., Purves, L.R., Adams, D.S., Hill, S., Leary, J.C., Weaver, H.A., Sandford, S.A., 2018. Development and testing of a pyro-driven launcher for harpoon-based comet sample acquisition. Acta Astronaut. 152, 218–228. https://doi.org/10.1016/j.actaastro.2018.07.045.

Waite, J.H., 2006. Cassini ion and neutral mass spectrometer: Enceladus plume composition and structure. Science 311, 1419–1422. https://doi.org/10.1126/science.1121290.

Wang, G.G., 2018. Moth search algorithm: A bio-inspired metaheuristic algorithm for global optimization problems. Memetic Comput. 10, 151–164. https://doi.org/10.1007/s12293-016-0212-3.

Witze, A., 2014. Icy Enceladus hides a watery ocean. Nature. https://doi.org/10.1038/nature.2014.14985.

Young, C., 1997. Penetration Equations. Technical Report SAND–97-2426, 562498. doi:https://doi.org/10.2172/562498.

Zipfel, P.H., 2007. Modeling and Simulation of Aerospace Vehicle Dynamics, second ed. American Institute of Aeronautics and Astronautics, Reston, VA. https://doi.org/10.2514/4.862182.